Dick: I wish we could have afforded to do this for the other two. Thanks for your conference reports. Marion

NUCLEAR INSTRUMENTS AND METHODS 154 (1978) 303-316 ; © NORTH-HOLLAND PUBLISHING CO.

CERENKOV COUNTER FOR SPACECRAFT APPLICATION

MARION C. RINEHART

Ford Aerospace & Communications Corp., 3939 Fabian Way, Palo Alto, California, U.S.A.

Received 2 January 1978

The design and performance of a Cerenkov telescope intended for the spectral analysis of protons and alphas from the GOES and TIROS spacecraft are described. Four proton data channels $E_p > 370$ MeV and two alpha channels $E_\alpha > 640$ MeV/nucleon are provided. The response to cyclotron protons in the 350–570 MeV range is described relative to: angular response, energy response, energy resolution, and counting efficiency. The response to sea-level muons is also presented.

1. Introduction

With the advent of routine commercial jetliner flights at higher altitudes – appropriate for the SST and the next generation of subsonic jets – attention has been drawn to the high altitude radiation environment which poses a potential health hazard for passengers and crew. To provide an improved data base on the enhancement of the high altitude radiation dose due to large solar flares, the NOAA plans to include monitoring instruments on four TIROS spacecraft (low altitude, near polar orbiters) and on three synchronous orbit GOES spacecraft. Since the high energy protons and alpha particles generated by solar flares produce the principal hazard to passengers at aircraft altitudes, a Cerenkov counter telescope has been chosen as the monitoring instrument.

The HEPAD (high energy proton and alpha detector) instrument provides four proton data channels, nominally 370–480, 480–640, 640–970, >970 MeV, and two alpha data channels, nominally 640–970 and >970 MeV/nucleon, all with a 4 s sample period. With a ≈ 1 cm^2 s view of the local zenith from TIROS, it provides a measure of the time dependent solar flare spectrum over the energy range allowed by the latitude-dependent rigidity cutoff. Except for near-polar latitudes, this cutoff lies above the instrument proton threshold at 370 MeV, so that the spectral data can provide the input to a calculation of the atmospheric dose transport under solar flare conditions. The data will also be of value in the study of solar flares and fast particle propagation through the interplanetary medium, allowing the development of better techniques for the prediction of near-term hazardous conditions for manned spacecraft and aircraft operations. The NOAA will make the data available to any interested party through its Space Environment Services Center at its Boulder, Colorado facility.

Section 2 describes the HEPAD design, while section 3 describes the HEPAD response to sea-level muons and various energy proton beams provided by the synchrocyclotron at the Space Radiation Effects Laboratory, Newport News, Virginia.

2. HEPAD design

2.1. Functional block diagram

Fig. 1 shows the division of the HEPAD functional elements between two mechanical subassemblies – the telescope which generates signals in response to ambient radiation, and the signal analyzer which

(1) identifies the particle type/energy category of telescope events,
(2) collects housekeeping information, and
(3) distributes power and commands from the DPU (Data Processing Unit).

In the telescope, each of two solid state detectors (SSD) supplies one analog signal to a charge-sensitive preamplifier in the signal analyzer, while the PMT supplies one analog signal derived from the anode and three analog signals derived from the last three dynodes. The high-voltage power supply generates PMT bias within the 1500–2700 V range linearly in response to a 0–5 V analog control voltage V_c generated in the command decoder in the signal analyzer, which provides $2^7 = 128$ equally spaced levels of the control voltage V_c. 0–5 V monitor signals derived from the Hi-V power supply and SSD bias are supplied to the signal analyzer. In addition, temperature is monitored on the PMT envelope by two redundant thermistors. +350 V SSD bias is provided by

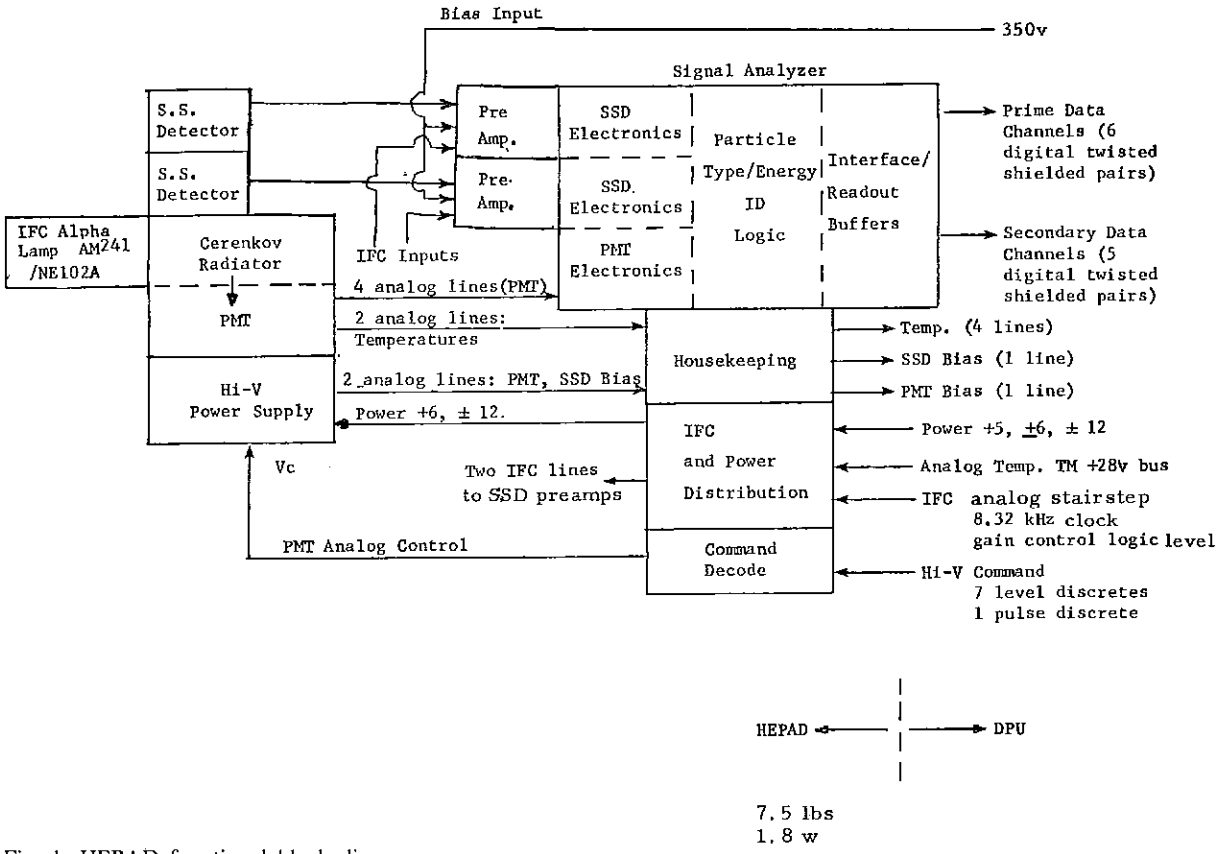

Fig. 1. HEPAD functional block diagram.

the DPU on a separate line, while IFC pulses are supplied to each preamplifier from the Signal Analyzer.

In the Signal Analyzer, the signals derived from solid state detectors and PMT are combined to produce eleven data channel readouts to the DPU: six prime data channels, P1–P4 identifying protons in four energy intervals and α 1–α2 identifying alphas in two energy intervals; and five secondary data channels S1–S5 employed to derive count-

TABLE 1

Data channel type	Data channel label	Observable	Count accumulation interval (nominal)	Nominal max. random rates (pps)
Primary	P1	protons 370–480 MeV	4 s	620
	P2	protons 480–640 MeV	4 s	420
	Ps	protons 640–970 MeV	4 s	260
	P4	protons >970 MeV	4 s	260
	α1	alphas 640–970 MeV/nucleon	4 s	80
	α2	alphas >970 MeV/nucleon	4 s	85
Secondary	S1	SSD #1 singles, LS 9	94 ms	1.8×10^5
	S2	SSD #2 singles, LS 7	94 ms	1.6×10^5
	S3	PMT singles, LS 1	94 ms	5.6×10^4
	S4	PMT gain monitor, LS 4 singles	2.5 s	2.0×10^3
	S5	LS 7, 9 double coincidences	1.2 s	2.0×10^4

rate corrections to the prime (coincidence) channel data, to identify malfunctions of telescope and signal analyzer components, and to measure the effective gain of the Cerenkov radiator/PMT. Two redundant thermistors are employed for temperature monitoring, as in the telescope.

The DPU supplies a 192 s, 1024 step, 0–8 V analog waveform, together with a 8.32 kHz S/C clock and a gain control logic level, to allow inflight calibration of electronic thresholds and coincidence counting efficiency. In the command decoder, seven level discrete command lines from the DPU are strobed by the pulse discrete line into a register which generates the 128 V_c levels.

The digital pulses on the eleven data channel outputs are accumulated for various time periods in counters located in the DPU. The counter content (19 bit binary) is sampled once every four sec-

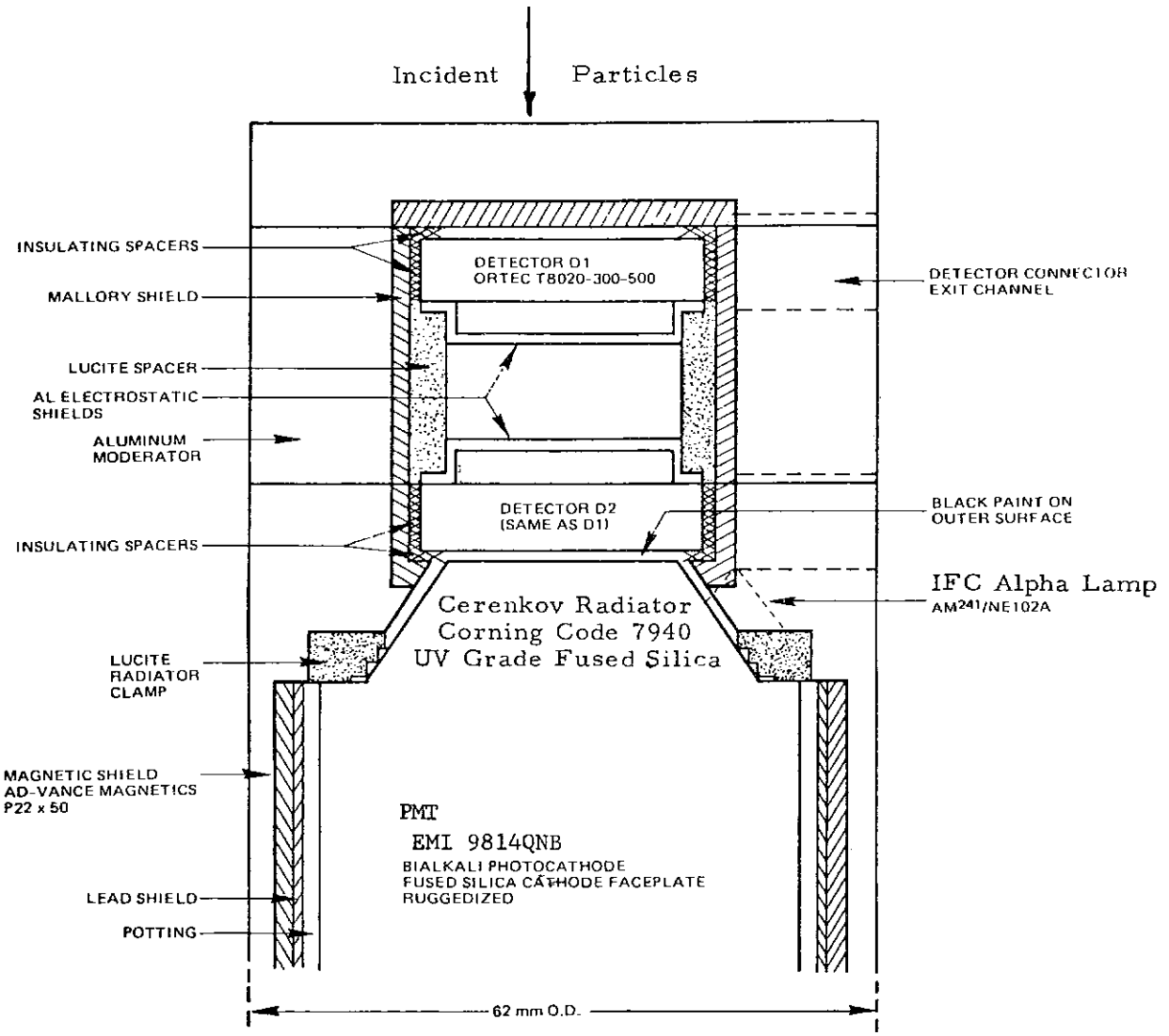

DETECTOR AREA: 3 cm^2
DETECTOR SEPARATION: 2.9 cm
GEOMETRIC FACTOR: G ≈ 0.9 cm^2-STER
ACCEPTANCE APERTURE: 68% OF G WITHIN ≤ 24° HALF-ANGLE
100% OF G WITHIN ≤ 34° HALF-ANGLE

Fig. 2. Telescope assembly.

onds. The readout format is in 8-bit floating point representation: 4 bits identifying the MSB, the remaining 4 bits reproducing the next most significant bits in the 19-bit counter (table 1). S1–3 identify events exceeding the most sensitive pulse height discriminator (level sensor, LS) thresholds associated with the two SSDs and the PMT, while S5 identifies time coincident events in the two SSDs which exceed these thresholds. S4 identifies those PMT events produced by the IFC alpha lamp (^{241}Am on NE102A) which exceed the fourth PMT LS threshold.

All housekeeping readouts are sampled once every 32 s, after encoding at 8 bits/sample.

2.2. Telescope design

Fig. 2 shows a plan view of the telescope assembly. Two surface barrier silicon detectors D1 and D2 (area 3 cm^2, thickness 500 μm, totally depleted) define an effective acceptance aperture of $\approx 24°$ half-angle or geometric factor ≈ 0.9 cm^{2}sr. All linear trajectories passing through these detectors also pass through the conical fused silica radiator (special PMT faceplate) which has an average thickness of ≈ 17 mm. For an isotropic environment, the probability distribution of pathlengths in the conical radiator has a mean value of 1.05 times the average thickness, so that the average Cerenkov radiation amplitude should correspond to traversal of ≈ 18 mm of silica. Silica is employed as the radiator to provide a convenient proton energy threshold (≈ 320 MeV) and to allow efficient transmission of the shorter wavelengths of the Cerenkov light (cutoff ≈ 1900 Å). Essentially all of the radiator's conical surface area is bare to allow total internal reflection of incident Cerenkov light from all trajectories with the acceptance cone. Assuming an average quantum efficiency of 18% and full light collection efficiency within the 2000–5500 Å interval, 220 photoelectrons should be produced by axial protons of $\beta = 1$.

Mallory metal (high-Z) is employed to shield the detectors against bremsstrahlung generated by ambient electrons (thickness is one absorption length for $E_\gamma < 350$ keV). Similarly, aluminum moderator (low-Z) is employed to shield these detectors against ambient electrons and protons and to suppress the bremsstrahlung radiated by the stopping electrons. Within the out-of-aperture solid angle, the moderator will stop protons of $\lesssim 80$ MeV and electrons of $\lesssim 7$ MeV. For in-aperture directions, the shielding is effective against protons of $\lesssim 65$ MeV and electrons of $\lesssim 4$ MeV and will absorb ≈ 10 MeV from a 370 MeV proton. Shielding of the detectors from "upward"-entering protons of $E \lesssim 90$ MeV is supplied by the silica radiator and the magnetic shield, lead shield and aluminum shell surrounding the PMT.

The Lucite spacer is used to position the detectors in the assembly, while insulating spacers prevent motion of the detector holders in a vibration environment and isolate signal ground (detector shell) from chassis ground. Similarly, the Lucite radiator clamp positions the PMT with respect to the SSD, contacting a very small fraction of the radiator area. The aluminum electrostatic shields protect the inner, biased surfaces of the SSDs from EMI capacitively coupled from the structure. To allow monitoring of the PMT quantum efficiency and gain during operation, a ^{241}Am alpha source (≈ 5 nci) coupled to a NE102A plastic scintillator (thickness 0.075 mm, diameter 5 mm)* is positioned near the silica radiator conical wall to illuminate the entire photocathode with fast light pulses of poorly defined amplitude ($\sim 30\%$ fwhm). The upbeam surface of the silica radiator is blackened to reduce the light collection efficiency for particle trajectories which intersect D1 and D2 but enter the telescope from the opposite direction.

Fig. 3 shows the nominal response of the silicon detectors and PMT to protons and alphas. The abscissa shows the energy lost in each silicon detector, while the ordinate shows the number of photo-electrons produced in the PMT. The trajectory for protons above 370 MeV is confined within the 125–500 keV abscissa range and the 21–500 photoelectron ordinate range, while the trajectory for alphas above 640 MeV/nucleon lies above the 500 keV and 500 photoelectron levels. The data handling circuitry associated with the telescope contains ten pulse height discriminators with thresholds at the abscissa and ordinate levels shown in fig. 3; protons are distinguished from alphas on the basis of LS8, 10 (silicon detectors) and LS5 (PMT). Energy analysis of each particle type is provided by the PMT LS1–6, while out-of-aperture events are suppressed by the requirement of a fast triple coincidence between LS1, 7, 9 before any event is counted. The table on fig. 3 shows the energy ranges of the data channels provided by the HEPAD and the discriminator

* Special NE130, Nuclear Enterprises, San Carlos, California.

coincidence logic employed to obtain these channels.

The silica radiator thickness is chosen sufficiently large so as to produce a PMT pulse height of ≈ 140 photoelectrons for 850 MeV protons, restricting the statistical fluctuation in this pulse height to about $\pm 10\%$ corresponding to an energy resolution of $850\ ^{+150}_{-110}$ MeV. At the correct PMTHV bias, the center of the ^{241}Am pulse height peak occurs at LS4, so that during quiescent periods the LS4 counting rate (S4 data channel) indicates a change in the overall PMT transfer function: silica transmission, PMT quantum efficiency, PMT gain. Observed changes in PMT gain are corrected by ground command of the HV bias, to return the S4 rate to a nominal ≈ 50 cts/s. Nominal PMT gain is $\approx 8 \times 10^6$.

The power supply is of the Cockroft–Walton type, providing 16 nominally equal ($\pm 5\%$) voltage increments; three are used between cathode and dynode #1, two are used between Dy #11 and #12, and one between the remaining adjacent pairs of electrodes. The anode voltage is set by exercise of 8 input command lines: seven level discrete lines (voltages set) and one pulse discrete line (strobe). The seven level discrete lines represent a standard 7 bit binary number, i.e. an integer N between 0 and 127, represented by the 0–5 V control voltage V_c varying linearly with N. The anode bias varies linearly with V_c within the 1500–2700 V range.

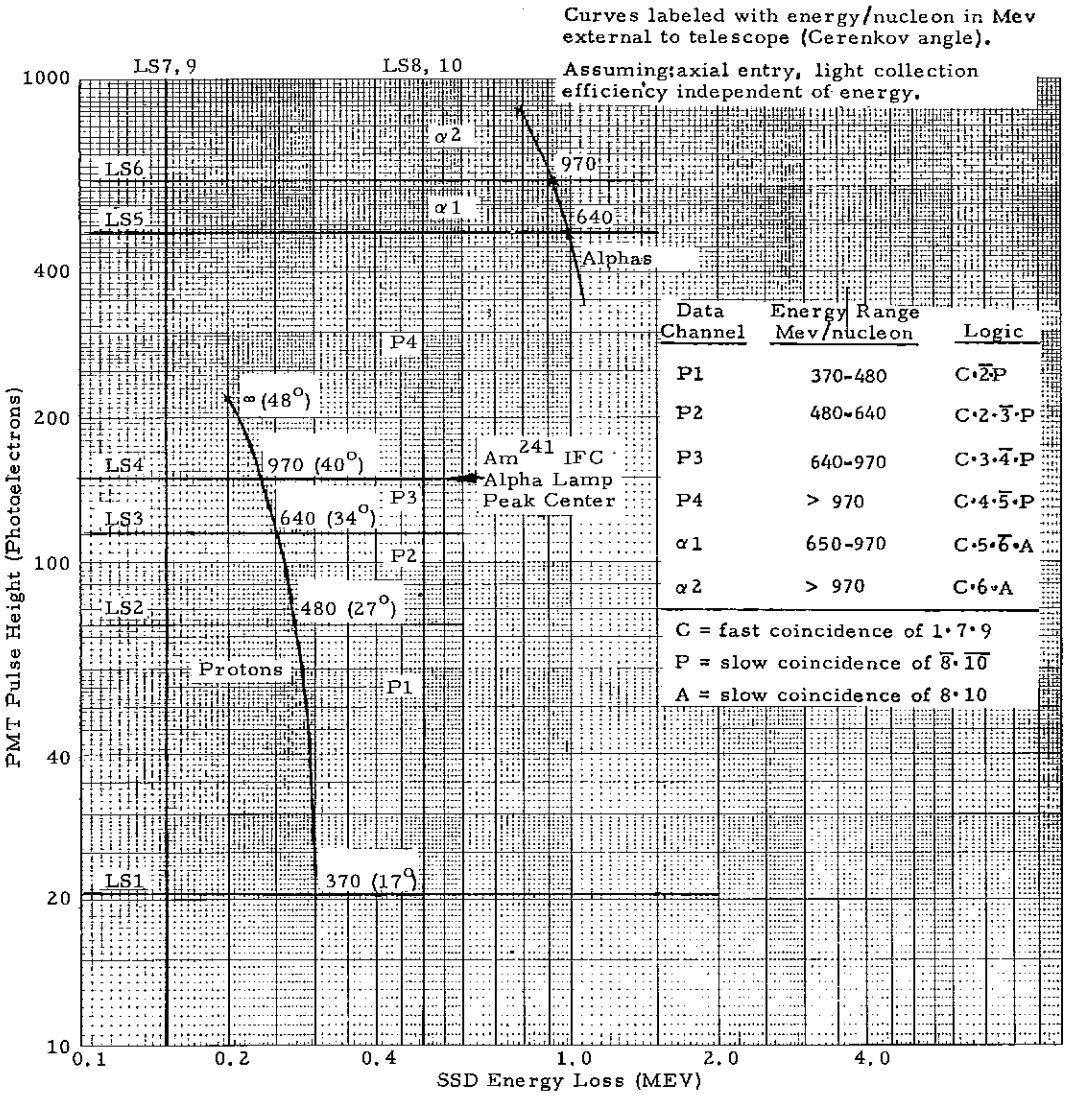

Fig. 3. Nominal telescope pulse height response.

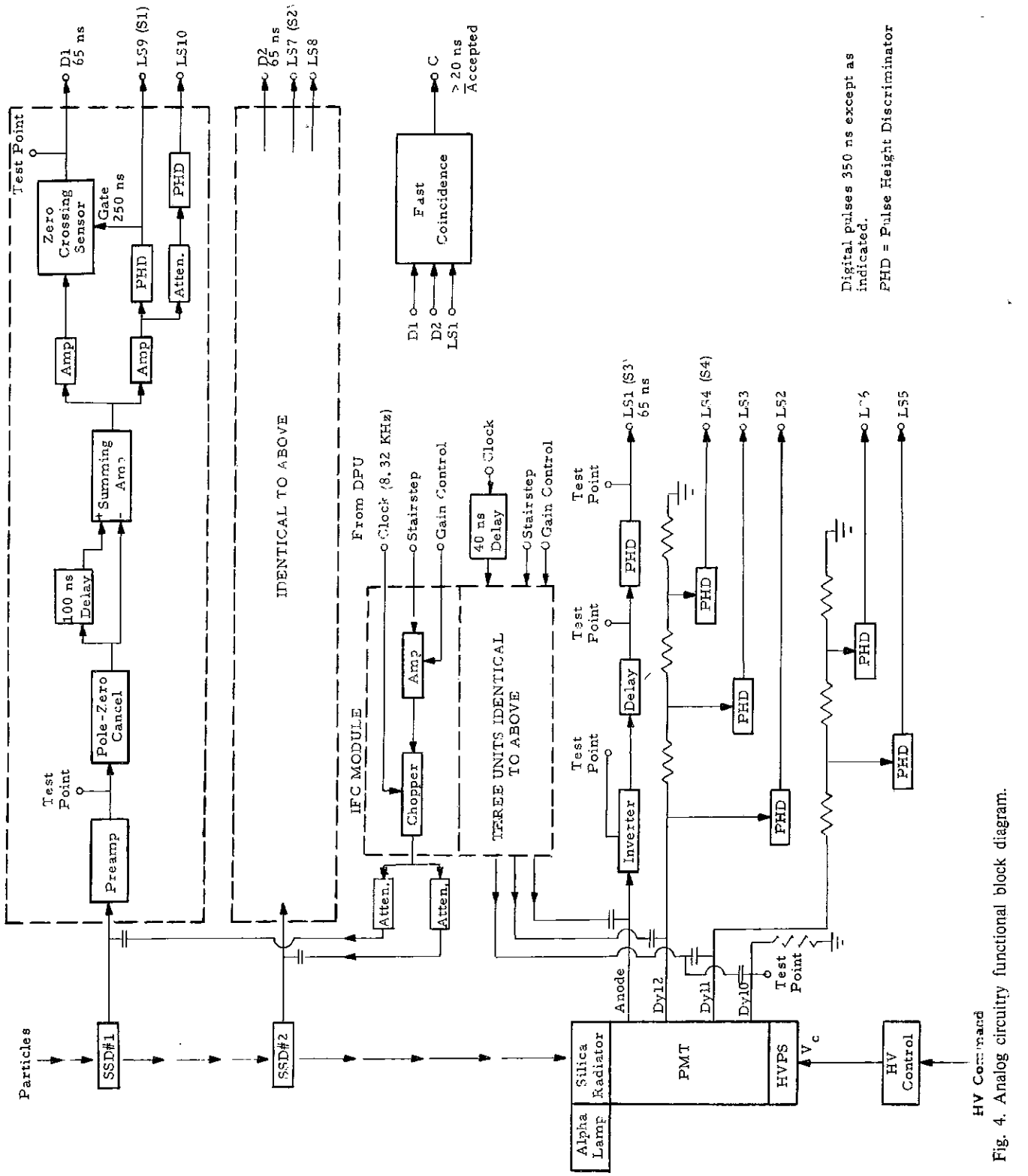

Fig. 4. Analog circuitry functional block diagram.

The change in electrode voltages from no-load to maximum load (20 μA anode current) is less than 0.25% for dynodes 1–7 and 0.5% for the remaining electrodes. The change in electrode voltages at maximum load due to variations in the +6, $\pm$12 V input power lines, temperature (nominal 5 °C $\pm$ 10 °C operating), and 8 h drift is less than 0.3% worst case. The combined noise and ripple voltage is $\leq$10 mV p–p, 0–50 MHz on the anode and $\leq$20 mV p–p, 0–50 MHz on any dynode, for bias voltage anywhere within its range and for no load or maximum load.

2.3. Signal analyzer design

Fig. 4 shows the pulse handling circuitry that processes the PMT and SSD analog pulses to produce the digital LS logic outputs which are combined as listed in fig. 3 to obtain the desired particle type/energy discrimination. Each SSD is followed by a charge sensitive preamp providing an output pulse of $\approx$25 ns risetime and $\approx$300 μs falltime, available at a test connector pin for pulse height analysis. A passive "pole-zero cancel" circuit reduces the falltime to $\approx$100 ns; this monopolar pulse is converted into a bipolar pulse in the summing amplifier, to provide a zero-crossing containing the information on event time. Two PHDs provide the LS9, 10 outputs at thresholds shown on fig. 3, responding to the $\approx$50 ns risetime positive portion of the bipolar signal pulse. The output of the LS9 PHD is read out as the S1 data channel, and is also used to gate "on" a "zero-crossing sensor" which generates a 65 ns digital pulse D1, 2 in response to the zero crossing of the bipolar signal pulse.

The PMT pulse height on dynodes 11, 12 is sensed by PHDs directly through resistive voltage dividers to obtain the LS2–6 thresholds shown on fig. 3. The anode pulse is first inverted before generating the 65 ns digital pulse LS1 (read out as data channel S3); this output is delayed to equalize the time of occurrence of D1, D2 and LS1 in response to a true triple coincidence event in the telescope. A fast coincidence circuit recognizes an overlap of $\geq$20 ns in D1, D2, LS1; its output strobes the slower type/energy analysis gates which implement the data channel logic shown on fig. 3. The D1, D2, LS1 signals are also available at a test connector to allow

(1) external generation of fast coincidences useful in gating MCA analysis of SSD and PMT pulse height distributions, and

(2) TAC/MCA measurements of the time-difference spectra of pairs of these signals.

To allow correction of the data channel counting efficiencies and energy boundaries for drifts in the electronics, a 192 s, 8.32 kHz train of IFC pulses is generated upon ground command and applied to all analog pulse lines to simulate true telescope events. Fig. 4 shows this pulse train for the SSD preamps derived through individual attenuators from a common chopper, which provides 8.32 kHz output pulses of $\approx$50 ns risetime and $\approx$9 μs decay time having an amplitude equal to its dc input. This input is derived from a swept 0–8 V waveform of 1024 equal steps spanning the 192 s period, with the amplifier gain selectable by a digital control signal. The pulse train to the PMT lines is obtained in an identical fashion, except that the clock pulses are delayed by 40 ns to compensate for the PMT transit time. The amplifier gains are chosen so that the pulse train amplitudes presented simultaneouslyto the SSD and PMT lines simulate telescope events in all data channels and provide visibility to all LS thresholds. These thresholds are identified by the times (within the 192 s stairstep interval) at which the data channels start or stop counting at the clock rate. Counting rates less than the clock rate can indicate a reduction in counting efficiency due to excessive walk or jitter in the digital inputs D1, D2, LS1 to the fast triple coincidence gate.

The particle type/energy ID logic section of the signal analyzer diagram of fig. 1 is implemented with overlap AND gates having the inputs shown in the fig. 3 table, where C represents the strobe of width between 20 ns and 65 ns and the remaining inputs are the 350 ns wide LS outputs shown on fig. 4. The output of these gates is stretched to a 400 ns width before transmission to the DPU for counting.

3. HEPAD performance

3.1. Experimental plan

To obtain the energy resolution and counting efficiency of the P1 data channel, the HEPAD was exposed to 360–570 MeV protons from the Space Radiation Effects Laboratory, Newport News, Virginia. The telescope was positioned $\approx$25 feet from the beam exit pipe, nominally on the beam line. The angle φ between the telescope axis and the beam line was varied to obtain the HEPAD response at five angles: $\varphi = 0°$, 12°, 21°, 27°, 32°.

The SSD and PMT pulse height spectra and counting efficiencies obtained at these angles were weighted and summed to represent the response to an isotropic environment. A pair of thin 2″ diameter plastic scintillators separated by 20′ were positioned on the beam line between the HEPAD and beam exit pipe; time-of-flight spectra were obtained at each beam energy to define the beam energy and energy width.

Typical TOF spectra allowed beam energy determination to better than 4–9 MeV (one channel at 0.1 ns/ch), with a fwhm of six times this value. A counter associated with the downbeam TOF scintillator was used as a beam monitor, controlling the accumulation period for the other counters. Beam intensities were typically a few hundred protons/cm^2 s, providing 10^5 monitor counts in 10–20 s. Accuracy of the counting efficiencies within the nominal data channel energy boundaries is limited to $\approx 1\%$ due to counting statistics and to $\approx 3\%$ due to φ setting accuracy. The accuracy of determination of pulse height spectral peaks is limited by drifts in PMT gain, external amplifier gain, and MCA analog circuitry; the data indicate an upper limit of $\pm 6\%$ for these effects.

During the runs, scalers recorded the counts from the eleven primary and secondary data channels (as listed in section 2.1); other counters recorded the rates of the D1, D2, LS1 signals (shown in fig. 4) as well as the D1·D2 coincidence rate which was generated external to the HEPAD from D1 and D2 signals stretched to 100 ns width. This external doubles rate at $\varphi = 0$ telescope orientation defined the beam intensity at the HEPAD, allowing calculation of absolute counting efficiency from the observed data channel rates.

3.2. Detector spectra

Figs. 5–8 show the PMT dynode 10 pulse height spectra for four beam energies, obtained by gating the MCA on an externally-formed D1·D2 fast double coincidence which lacks any pulse height requirement on the PMT pulse. At each energy, the spectra for five discrete φ values are shown together with the "weighted-sum spectrum" representing the response to an isotropic environment. The reduction in spectrum area with increasing φ corresponds to the reduction in projected overlap area A_p of the two SSDs which is presented to particles entering the telescope at φ:

$$A_p/A = 2\cos\varphi\,[\cos^{-1}x - x\sqrt{(1-x^2)}]/\pi, \qquad (1)$$

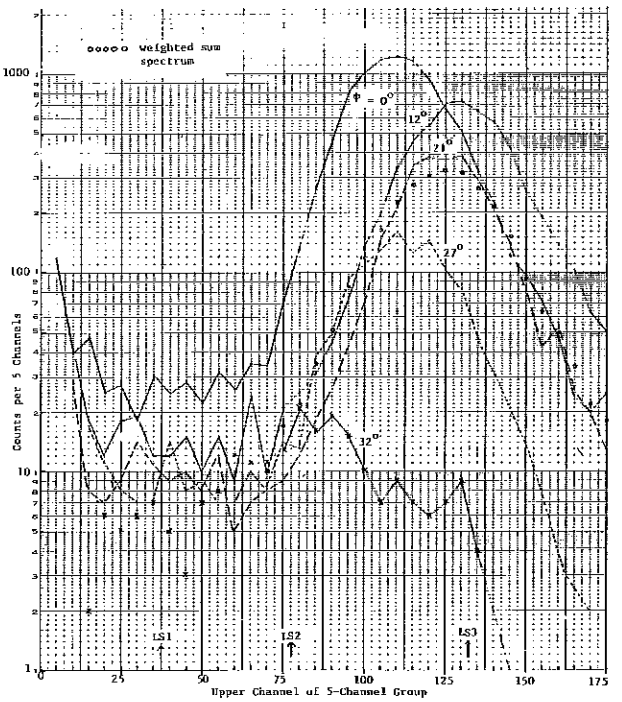

Fig. 5. Dynode 10 spectra at 561 MeV vs. ϕ.

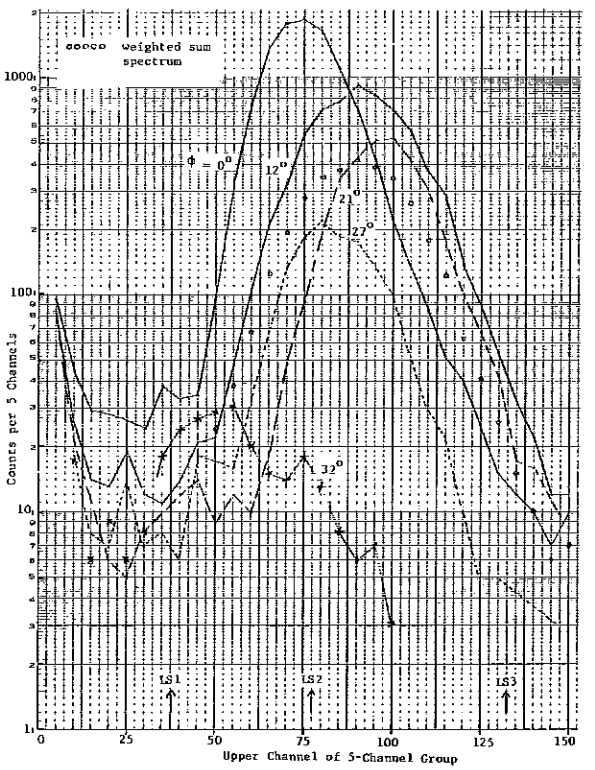

Fig. 6. Dynode 10 spectra at 474 MeV vs. ϕ.

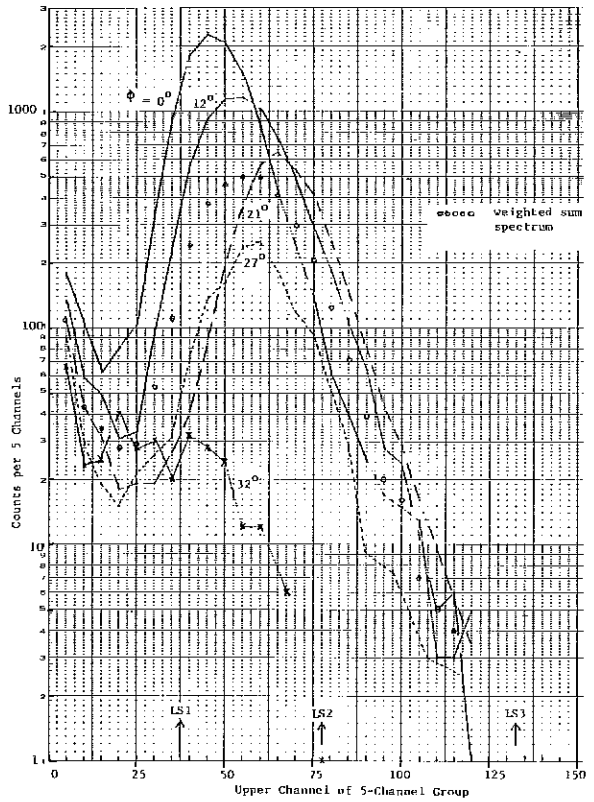

Fig. 7. Dynode 10 spectra at 412 MeV vs. ϕ.

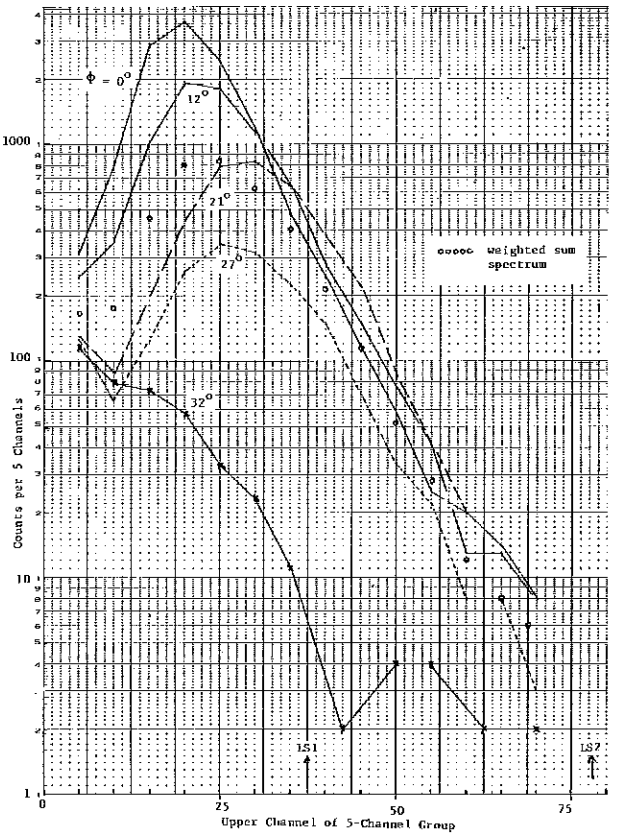

Fig. 8. Dynode 10 spectra at 368 MeV vs. ϕ.

where $x = \tan\varphi/\tan\eta$, η = angle to telescope axis of extreme ray of acceptance aperture = 34° (nominal), A = SSD area = 3.0 cm² (nominal). For all energies, the spectrum area closely follows this expected φ dependence. The largest mean pulse height occurs for the $\varphi = 12°$ or 21° spectrum; the peak of the weighted sum spectrum corresponds to that of a discrete angle spectrum in the $\varphi = 12°$ to 21° range. The relative width (fwhm ÷ peak) minimizes for the $\varphi = 21°$ spectrum.

Spectra taken at intermediate energies and at $\varphi = 0$ showed peak channels and relative widths interpolated between values in table 2 at these four energies. The relative widths for the $\varphi = 0°$ spectra are consistent with statistical broadening and beam energy width broadening if the mean pulse height at 561 MeV corresponds to a mean of ≈ 100 photoelectrons, suggesting that the light collection efficiency is essentially independent of Cerenkov angle for axial entry. On the other hand, the relative widths of the weighted-sum spectra reflect the indicated strong dependence of light collection efficiency on φ.

Fig. 9 shows the φ dependence of the SSD #2 pulse height spectra (preamp output) at 570 MeV

TABLE 2

E (MeV)	$\varphi = 0°$ peak chan.	$\varphi = 0°$ relative width	$\varphi = 12°$ peak chan.	$\varphi = 12°$ relative width	$\varphi = 21°$ peak chan.	$\varphi = 21°$ relative width	$\varphi = 27$ peak chan.	$\varphi = 27$ relative width	Weighted sum peak chan.	Weighted sum relative width
368	16.9	0.81	20	0.87	26	0.75	24	0.87	22	0.92
412	44	0.49	51	0.54	62	0.38	56	0.45	54	0.59
474	71	0.35	87	0.40	95	0.30	80	0.38	88	0.43
561	108	0.32	128	0.28	121	0.27	110	0.34	122	0.32

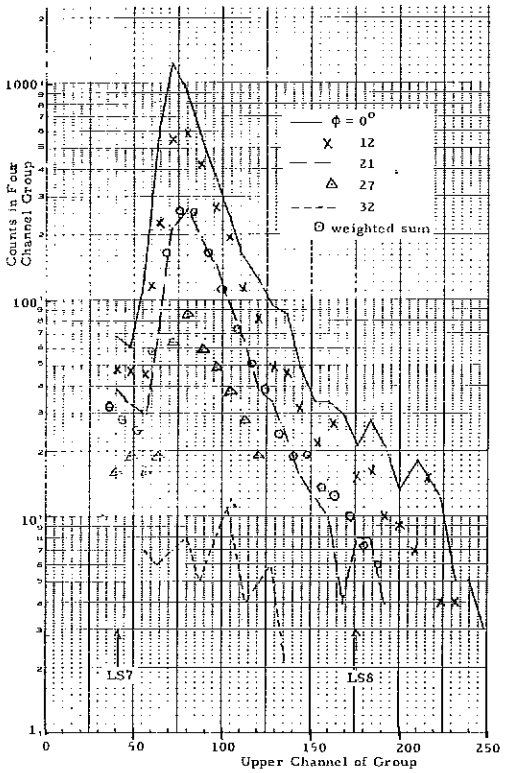

Fig. 9. SSD#2 response at 570 MeV.

beam energy, together with the weighted-sum spectrum. These spectra were obtained by gating the MCA on an externally formed D1·LS1 fast double coincidence, which lacks any pulse height requirement from the SSD #2 pulse. Essentially identical spectra were obtained from SSD #1, obtained with D2·LS1 gating of the MCA. The spectrum area shows the expected strong φ dependence as for the figs. 5–8 spectra, and the weighted-sum spectrum is well represented by the $\varphi \approx 20°$ spectrum. The area under the weighted sum spectrum above the LS8 threshold at channel 174 constitutes $\approx 3\%$ of the total area. The SSD #1 spectrum shows the same relative area above its higher discriminator LS10, so that $\approx 6\%$ counting efficiency loss is expected at 570 MeV due to the $\bar{8}\cdot\bar{10}$ logic requirement for proton counting.

Similar spectra obtained at lower energies show an increase in peak pulse height with decreasing energy; all $\varphi = 0°$ spectra show relative widths ($\approx 35\%$) somewhat larger than the asymptotic Landau relative fwhm of $\approx 30\%$, reflecting detector noise levels of ≈ 30 keV (0.5 μs integration, 0.5 μs differentiation). The weighted sum spectrum at all energies has a relative fwhm of $\approx 40\%$, reflecting the nominal sec φ dependence of the mean pulse height.

3.3 Energy response

Spectra similar to figs. 5–8 were obtained at many energies in the 351–572 MeV range. Fig. 10 shows the experimental values for the peak channel of the dynode 10 spectrum (for $\varphi = 0°$) plotted

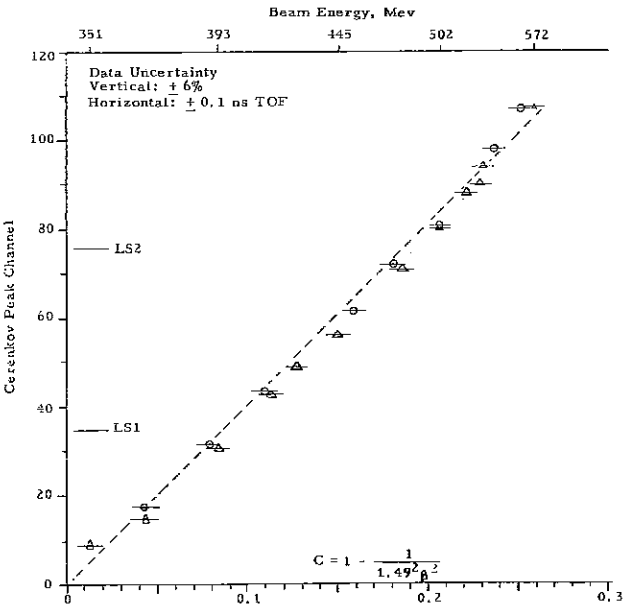

Fig. 10. Axial energy response.

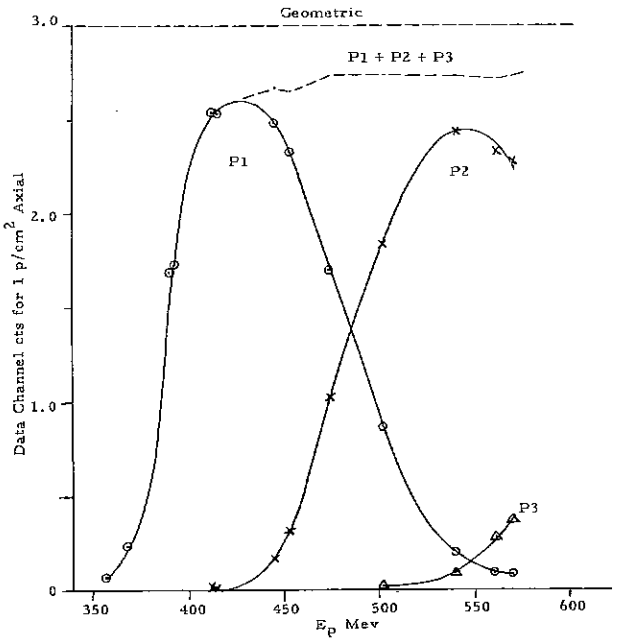

Fig. 11. Data channel counting efficiencies; Counts/sec for 1 p/cm² sec axial.

against the quantity $C = 1 - 1/n^2\beta^2$, with refractive index $n = 1.49$ and $\beta = V/C$ at the center of the silica radiator. Since C is proportional to the theoretical number of Cerenkov photons emitted per unit pathlength, the points should nominally fall on a straight line passing through the origin for the proper choice of numerical value for the refractive index. Fig. 10 shows that the choice of $n = 1.49$ provides a good fit of the data points to the dotted line; this effective refractive index is consistent with a comparison of $n(\lambda)$ with the combined wavelength dependence of the Cerenkov light production, silica transmission, and quantum efficiency. The fig. 10 fit also suggests the absence of significant effects due to energy dependence of the light collection efficiency, silica fluorescence, or Cerenkov light production by secondary particles generated by the incident protons. A similar plot of the peak channels of the weighted-sum spectra (from table 2) vs $C(\beta)$ also shows an excellent linear fit using the same choice $n = 1.49$.

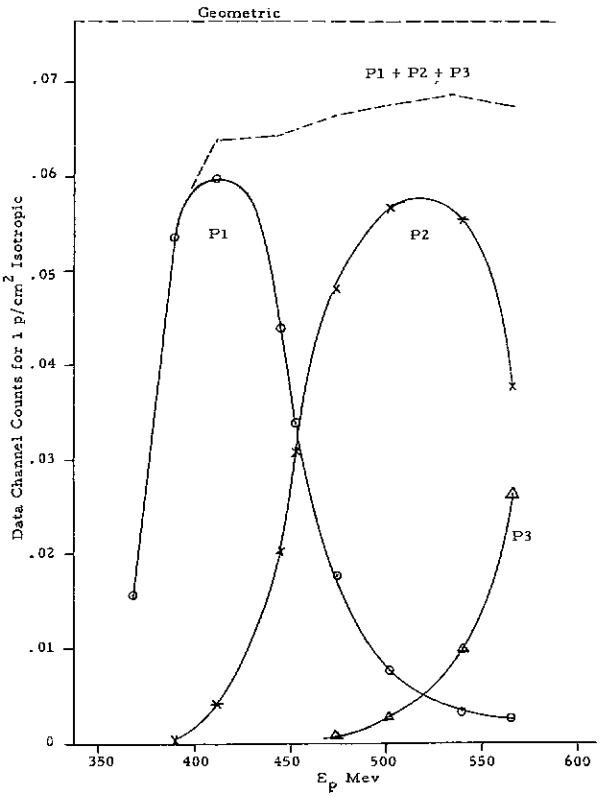

Fig. 12. Data channel counting efficiencies; Counts/sec for 1 p/cm^2 sec isotropic.

3.4. Energy resolution

Fig. 11 shows the experimental counting efficiency vs energy at the P1–3 data channels for axial protons. The lower energy boundary of P1 at ≈ 380 MeV is established by the LS1 threshold, while the common boundary of P1 and P2 at ≈ 480 MeV is set by the LS2 threshold. The slope of the P1, 2 responses near 480 MeV reflects the relative width of the fig. 6 $\varphi = 0$ spectrum, as well as the energy dependence of $C(\beta) = 1 - 1/n^2\beta^2$. The steeper slope of the P1 response near 380 MeV reflects the stronger energy dependence of $C(\beta)$ near the silica Cerenkov threshold. The sum of the three responses P1 + P2 + P3 is shown relative to the geometric sensitivity (SSD nominal area of 3 cm^2). At the higher energies, this sum differs by $\approx 9\%$ from the geometric value, of which 6% is due to the $\bar{8} \cdot \bar{10}$ logic requirement as cited in section 3.2 above. Moreover, SSD spectra at 397 MeV show that an 8% reduction is expected from this $\bar{8} \cdot \bar{10}$ requirement at this energy. As shown in the fig. 7 $\varphi = 0$ spectrum for 412 MeV, a portion of the spectrum is excluded by the LS1 requirement for the lower energies, so that the P1–3 sum does not reach the 91% asymptote below ≈ 450 MeV. The remaining 3% discrepancy in the P1–3 sum is within the 5% uncertainty in the SSD area.

Fig. 12 shows the expected response for an isotropic environment, calculated as a weighted sum of the response at five discrete angles. Compared to fig. 11, the data channel energy boundaries occur at lower energies – reflecting the larger mean pulse heights at $\varphi > 0$ relative to $\varphi = 0$ pulse heights as shown in figs. 5–8. The asymptote of the P1–3 sum is $\approx 89\%$ of the geometric value of .0765; this value is obtained as a weighted sum of the experimental values of A_p in the same manner as the data points are obtained from the experimental values of the data channel counts. The 11% discrepancy between the geometric value and the asymptotic value of the P1–3 sum can be understood as: 6% due to the $\bar{8} \cdot \bar{10}$ logic requirement, 3% due to the SSD area as obtained from the axial data of fig. 11, and 2% due to inaccuracies in the weighting/summing algorithm.

The differences between the fig. 12 energy-band boundaries (377, 453, and 570 MeV) and the nominal values (370, 480 and 640 MeV) reflect inaccuracies in the settings of the LS 1–3 thresholds for the chosen PMT high-voltage bias. A linear fit to the weighted-sum peaks of table 2 can be used to

estimate the changes in energy band boundaries for any given change in PMT gain or LS thresholds.

3.5. Coincidence timing

The D1, D2, LS1 signals used within the HEPAD to form the fast triple-coincidence strobe were also available externally for timing analysis. Since excessive walk/jitter in these signals can reduce the fast coincidence efficiency, the walk/jitter in the three signal pairs D1/D2, D2/LS1, D1/LS1 were obtained with a TAC/MCA at proton beam energies of 397, 477, 525, 570 MeV for comparison with the timing characteristics under IFC pulse stimulation. The signal timing within the HEPAD is adjusted so that these three 65 ns wide signals are within a few ns of coincidence for IFC pulses having amplitudes simulating $\beta \approx 1$ proton events (channel P4) in the telescope.

Fig. 13a shows the results for the shift in the TAC spectrum peak (walk) at the four proton energies relative to the peak position using IFC stimulation. The curves are labelled with the appropriate TAC start/stop signals. The "zero-crossing timing" technique used for generating the D1, D2 signals provides essentially no energy dependence to the D1, D2 mean separation. The "leading edge timing" technique used for generating the LS1 signal produces a walk of ≈ 10 ns at 397 MeV, representing a delay in LS1 formation which is comparable with the 5-10 ns rise time of the anode-current pulse.

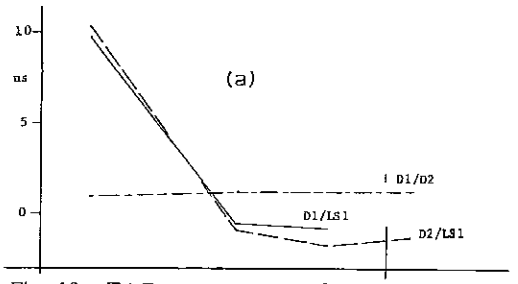

Fig. 13a. TAC spectrum peak from protons.

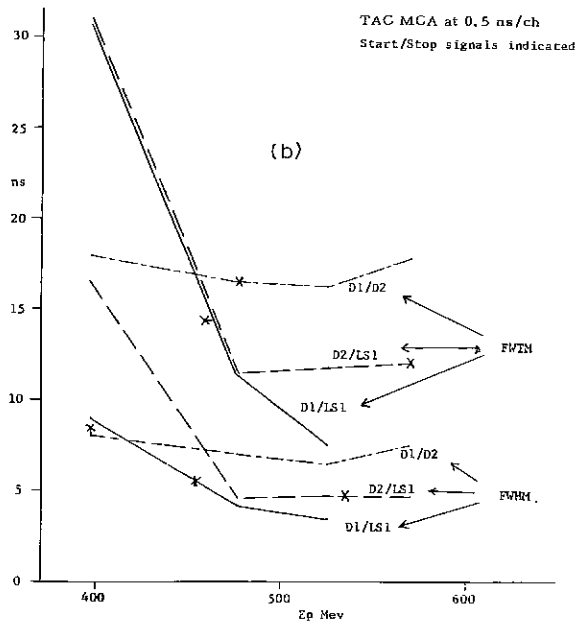

Fig. 13b. TAC spectrum widths from protons.

Fig. 13b shows the results for the fwhm and full-width-at-tenth-maximum (fwtm) of the same TAC spectra. The higher noise of the SSDs compared with the PMT appears as a broader peak for the D1/D2 spectra. The ratio of the fwtm÷fwhm is generally ≈ 2.4, considerably greater than the ≈ 1.8 value characteristic of a Gaussian. The larger values at 397 MeV for the spectra including LS1 probably reflect the greater sensitivity to noise in the leading-edge timing technique for pulses generally near the LS1 threshold. The "X" attached to each curve indicates the width of the TAC spectrum obtained under IFC stimulation, and is generally similar to the experimental values at the higher energies.

At 397 MeV, the half-width-at-tenth-maximum values of ≈ 15 ns and ≈ 9 ns for the three pulse pairs are considerably less than the ≈ 45 ns timing offset allowed before rejection of the event in the HEPAD fast coincidence gate. Consequently, the observed timing jitter should produce an insignificant coincidence inefficiency at all energies, even when the fig. 13a walk of ≈ 10 ns at 397 MeV is included. This conclusion is consistent with the close correspondence between the P1–3 sum and the geometric counting efficiencies (after accounting for the effect of the $\bar{8}\cdot\bar{10}$ logic requirement) shown on figs. 11 and 12.

3.6. Response to muons

On two occasions during the ≈ 1 week calibration at SREL, the HEPAD was oriented to view the zenith through ≈ 1000 gm/cm^2 of cement and allowed to accumulate counts over a 10–12 h period. Fig. 14 shows the Dy 10 spectra obtained relative to the LS1–3 thresholds; the signal gain is reduced to ≈ 0.4 of the value used for figs. 5–8. The 2/25 spectrum shows a relative width consistent with that of the weighted-sum spectrum at 561 MeV, while the 2/23 spectrum indicates a

drift of PMT gain occurred during the ≈10 h accumulation resulting in a broader peak centered at a higher channel. If the mean peak channel = 85.5 is identified with $\beta = 1$ muons, this pulse height is ≈16% less than expected from an extrapolation of a linear fit of the table 2 weighted-sum peaks plotted vs $C(\beta)$, suggesting a reduction of ≈16% in the light collection efficiency for $\bar{\beta} \approx 1$ events (48° Cerenkov angle) relative to that for the $\bar{\beta} \approx 0.78$ events (31° Cerenkov angle) at 560 MeV. The TAC spectrum for the D1/D2 pair taken for the 2/23 run shows the same walk but a somewhat smaller width than the spectra for higher energy protons summarized on fig. 13.

The triple-coincidence D1·D2·LS1 event rate for these overnight muon runs was ≈20 cts/h, with the D1·D2 doubles rate ≈22 cts/h. A triple-coincidence rate of ≈40 cts/h is normally observed in the FACC laboratory environment, which has a much thinner overhead moderator (building roof). Such muon runs provide a convenient means of verifying overall instrument performance, including coincidence counting efficiency and PMT gain drift. If the PMT bias is reduced to place the muon peak between, for example, LS2 and LS3 thresholds, the number of P1, P2 and P3 data channel output counts occurring during the muon run can be compared with the number of counts in the MCA memory stored in the channels corresponding to the LS1–2, LS2–3, LS3–4 intervals respectively. If the number of data channel counts is less than the number in these MCA

Date	Accum. Period	Pulse Height Spectrum Peak	FWHM	FWHM / Peak	D1/D2 TAC Spectrum Walk	FWHM	FWTM
2/23	~ 600 Min.	ch88	35ch	.40	-1 ns	3-4 ns	~16 ns
2/25	~ 750 Min.	ch83	27ch	.33	—	—	—

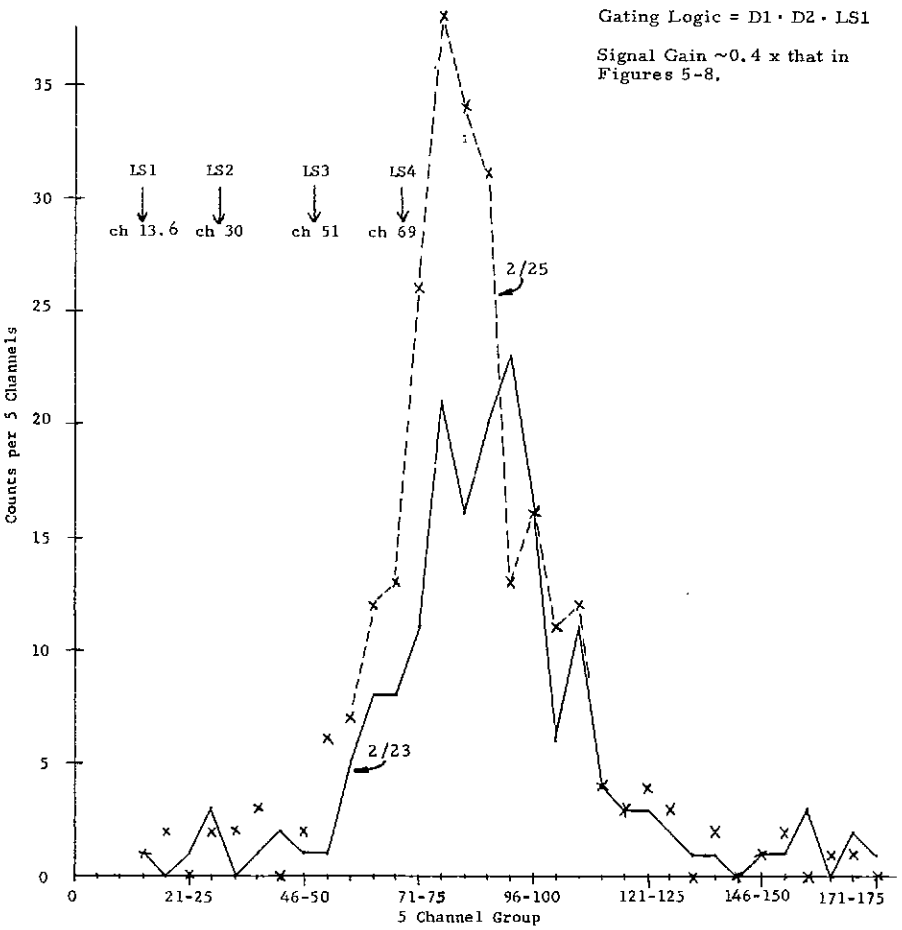

Fig. 14. Dynode 10 spectra from muons.

intervals, anomalous performance of the data channel logic or excessive walk/jitter in the strobe gate inputs is indicated.

4. Summary

The principal performance features of the HEPAD can be summarized as follows:

- angular response: Consistent with the theoretical SSD projected overlap area vs φ as given by eq. (1);
- energy response: For E_p in 370–570 MeV range, (1), the Cerenkov peaks closely follow the theoretical β dependence with effective $n = 1.49$, consistent with no energy-dependence to light collection efficiency for both axial and isotropic protons, and (2) the nominal Cerenkov pulse height for isotropic protons is $\approx 20\%$ greater than that for axial protons. For 570 MeV protons, the nominal Cerenkov pulse height for axial entry corresponds to ≈ 100 photoelectrons, consistent with an average quantum efficiency of 18% and full light collection efficiency. For cosmic-ray muons, the Cerenkov peak is 10–20% lower than expected for isotropic $\beta = 1$ particles, implying a similar reduction in light collection efficiency for 48° Cerenkov emission angles;
- energy resolution: Limited by the relative widths of the Cerenkov spectra. For axial protons, the relative widths are consistent with statistical fluctuations about the nominal mean values, where the variance is taken as $1.6 \times$ mean number of photoelectrons – to include fluctuations in the PMT gain and in the number of photons generated. For isotropic protons, the relative widths are larger than for axial protons, reflecting a strong φ dependence for the Cerenkov peaks;
- counting efficiency: For the differential energy channels P1, 2 the peak counting efficiency is $\approx 80\%$ of geometric, limited by the pulse-height discriminator window width relative to the width of the Cerenkov pulse height peak. For the sum of P1–3, the counting efficiency is $\approx 90\%$; of the 10% discrepancy, 6% is attributable to the Landau tail of the SSD pulse-height distribution.

I wish to thank R. Grubb of the NOAA for constructive comments and criticism during the development of the instrument. I am grateful to Dr. R. Siegel of SREL for his accomodating spirit in making the SREL facility available, and to the SREL staff for their cheerful and expert cooperation. I am particularly grateful to Dr. W. Kolasinski and Dr. B. Blake at Aerospace Corporation for their initial recommendation of a three-element telescope design and for their generous assistance in the design, execution, and interpretation of the cyclotron calibrations.